

Research Article

Open Access



Equivalent doping of Te leads to optimized electrical and thermal transport properties in thermoelectric $\text{Cu}_2\text{MnSnSe}_4$ alloys

Fulong Liu, Yuqing Sun, Zhihao Li, Panpan Peng, Chunlei Wang, Hongchao Wang

School of Physics, State Key Laboratory of Crystal Materials, Shandong University, Jinan 250100, Shandong, China.

Correspondence to: Dr. Hongchao Wang, School of Physics, State Key Laboratory of Crystal Materials, Shandong University, No. 27 Shanda South Road, Jinan 250100, Shandong, China. E-mail: wanghc@sdu.edu.cn

How to cite this article: Liu, F.; Sun, Y.; Li, Z.; Peng, P.; Wang, C.; Wang, H. Equivalent doping of Te leads to optimized electrical and thermal transport properties in thermoelectric $\text{Cu}_2\text{MnSnSe}_4$ alloys. *Microstructures* 2025, 5, 2025043. <https://dx.doi.org/10.20517/microstructures.2024.125>

Received: 15 Nov 2024 **First Decision:** 19 Dec 2024 **Revised:** 3 Jan 2025 **Accepted:** 21 Jan 2025 **Published:** 17 Apr 2025

Academic Editor: Zhigang Chen **Copy Editor:** Fangling Lan **Production Editor:** Fangling Lan

Abstract

Quaternary chalcogenides have garnered considerable interest within the field of thermoelectric due to their intrinsic low thermal conductivity, wide bandgap and high element enrichment advantages. In this work, the thermoelectric performance of $\text{Cu}_2\text{MnSnSe}_4$ was enhanced by co-optimizing the carrier concentration and lattice thermal conductivity through self-doping with Cu and doping with Te. A series of $\text{Cu}_2\text{MnSnSe}_4$ and $\text{Cu}_{2.1}\text{Mn}_{0.9}\text{SnSe}_{4-x}\text{Te}_x$ ($x = 0, 0.01, 0.05, 0.10$) samples were prepared by ball-milling and hot-pressing methods. The carrier concentration of the samples was significantly increased after Cu self-doping, leading to optimized electrical transport performance. The notable reduction in lattice thermal conductivity was attributed to the scattering effect caused by Te substitution-induced point defects. At 673 K, the lattice thermal conductivity of the $\text{Cu}_{2.1}\text{Mn}_{0.9}\text{SnSe}_{3.9}\text{Te}_{0.1}$ sample obtained the lowest value of $0.62 \text{ W m}^{-1}\text{K}^{-1}$. Finally, it achieved a maximum $zT \sim 0.5$ at 673 K in the $\text{Cu}_{2.1}\text{Mn}_{0.9}\text{SnSe}_{3.9}\text{Te}_{0.1}$ sample, roughly twice that of the $\text{Cu}_2\text{MnSnSe}_4$ sample.

Keywords: $\text{Cu}_2\text{MnSnSe}_4$ alloys, Te-doping, electrical properties, thermal conductivity, thermoelectric performance

INTRODUCTION

The energy crisis and environmental concerns have consistently driven the pursuit of sustainable energy. An increasing number of advanced energy materials, such as dielectric high entropy energy materials, solar



© The Author(s) 2025. **Open Access** This article is licensed under a Creative Commons Attribution 4.0 International License (<https://creativecommons.org/licenses/by/4.0/>), which permits unrestricted use, sharing, adaptation, distribution and reproduction in any medium or format, for any purpose, even commercially, as long as you give appropriate credit to the original author(s) and the source, provide a link to the Creative Commons license, and indicate if changes were made.



cell energy materials and lithium-ion battery energy materials, have attracted widespread attention^[1-3]. Additionally, thermoelectric materials and devices can convert waste heat into electric energy without causing environmental pollution, thus providing a new solution for alleviating the energy crisis and promoting green renewable energy^[4,5]. However, the search for high-performance thermoelectric materials is a major obstacle to the widespread application of thermoelectric technology on a large scale^[6]. The properties of thermoelectric materials are determined by the dimensionless figure of merit ($zT = S^2\sigma T/\kappa_{\text{tot}}$), where $S^2\sigma$ stands for the power factor (PF), T stands for the absolute temperature, and κ_{tot} indicates the total thermal conductivity ($\kappa_{\text{tot}} = \kappa_L + \kappa_e$, where κ_e and κ_L refer to electronic and lattice thermal conductivity, respectively). It is evident that a thermoelectric material with excellent performance should keep high PF and low κ_{tot} , but these parameters are interrelated^[7]. Achieving optimal electrical and thermal transport performance simultaneously is challenging, making it difficult to attain a satisfactory zT ^[7,8]. Over the past two decades of research, many strategies have been successfully implemented in existing systems (Bi_2Te_3 , PbTe , and GeTe)^[9-12] to optimize thermoelectric parameters and increase zT , such as modulation doping^[13,14], energy band engineering^[15,16] and energy filtering effects^[17], to optimize electrical transport performance; entropy engineering^[18,19], defect engineering^[20,21] and nanoengineering^[22,23] are used to optimize thermal transport performance.

The development of high-performance thermoelectric materials should focus on not only optimizing existing systems, but also developing potential thermoelectric materials. Elements-rich quaternary chalcogenides have attracted widespread attention due to their intrinsic low thermal conductivity^[24]. The crystal structure of quaternary chalcogenide is derived from a ZnSe supercell arranged in a double-periodic manner along the Z axis, with the Zn site being substituted by three different cations^[25]. With the mismatch of atomic size between the substituting elements, Se atoms deviates from the original ideal tetrahedral position, resulting in lattice distortion and modification of the crystal structure from high-symmetry cubic structure to low-symmetry non-cubic structure, which is conducive to enhancing phonon scattering and inhibiting κ_L ^[26,27]. Quaternary chalcogenides have a pseudocubic crystal structure and use the structural distortion parameter ($\eta = c/2a$, where c and a are lattice parameters along the z -axis and x -axis, respectively) to reflect their symmetry of crystal structure. Quaternary chalcogenides with η close to 1 usually have better electrical properties^[26]. The reduction of the crystal structure's symmetry can disturb the original periodicity of the lattice and deteriorate the electrical performance. Therefore, preserving the symmetry of the crystal structure is crucial for the thermoelectric properties. $\text{Cu}_2\text{MnSnSe}_4$ has been discovered in recent years but it has a relatively wide bandgap (0.7 eV) and poor electrical performance^[27], which limits zT . Many previous studies have successfully optimized $\text{Cu}_2\text{MnSnSe}_4$ carrier concentrations (n_H) through the non-stoichiometric Cu ^[27] and In doping^[28]. Additionally, we have made progress in regulating the low thermal conductivity of $\text{Cu}_2\text{MnSnSe}_4$ by manipulating configurational entropy^[19] and lattice strain^[29]. However, there remains considerable potential for further enhancement of thermoelectric performance. In addition, it can be found that Te doping is particularly interesting and effective in many alloys for improving their thermoelectric performance. Some classical XTe ($\text{X}:\text{Bi}, \text{Sn}, \text{Pb}$)^[9-12] alloys have also achieved cutting-edge zT due to their unique band properties and crystal structures. Therefore, the equivalent doping of Te can further optimize the thermoelectric performance of $\text{Cu}_2\text{MnSnSe}_4$.

In this work, the electrical and thermal transport properties of $\text{Cu}_2\text{MnSnSe}_4$ were simultaneously optimized through self-doping with Cu and doping with Te . A series of samples, including $\text{Cu}_2\text{MnSnSe}_4$ (S-1) and $\text{Cu}_{2.1}\text{Mn}_{0.9}\text{SnSe}_{4-x}\text{Te}_x$ ($x = 0, 0.01, 0.05, 0.10$; S-2 to S-5), were prepared. An analysis was conducted on their crystal structures and electrical and thermal transport properties. At 673 K, the $\text{Cu}_{2.1}\text{Mn}_{0.9}\text{SnSe}_{3.9}\text{Te}_{0.1}$ sample obtained the lowest κ_L of $0.6 \text{ W m}^{-1}\text{K}^{-1}$. Within the measured temperature range, all doped samples exhibited enhanced zT . Ultimately, the $\text{Cu}_{2.1}\text{Mn}_{0.9}\text{SnSe}_{3.9}\text{Te}_{0.1}$ sample obtained a maximum zT of ~ 0.5 at 673 K,

representing approximately twice that of the $\text{Cu}_2\text{MnSnSe}_4$ sample.

EXPERIMENTAL SECTION

The elements Cu, Mn, Sn, Se, and Te (Aladdin, powder, purity > 99.9%) were weighed out in atomic proportions of S-1 to S-5 and then placed in a stainless steel tank (this was done in a glove box under an argon atmosphere). The tank was placed on a high-energy ball-milling machine and run for 10 h at 500 rpm. After the operation, the powder was placed into a graphite tool for hot pressing under vacuum at 873 K and a pressure of 60 MPa for 1 h. After the hot pressing, the sample, which had cooled to room temperature, was taken out and re-ground into powder form. The hot-pressing operation was repeated under the same conditions. Finally, a high-density disc-shaped sample was obtained.

The chemical compositions and phase structures of the sample powder were analyzed by Rigaku Smartlab X-ray diffractometer with Cu $K\alpha$ radiation. The samples were refined using the Fullprof software for Rietveld refinements. The microstructure of the samples was analyzed by scanning electron microscopy (SEM; JSM-7610F). The valence state of the sample elements was analyzed using X-ray photoelectron spectroscopy (XPS) by Thermo Scientific K-Alpha instrument. The electrical conductivity (σ) and Seebeck coefficient (S) of the samples were tested by the LINSEIS LSR-3 instrument, within a temperature range from 323 to 673 K. The thermal diffusion coefficient (D) was tested by a laser flash method (TA, DLF-1200). The experimental density (ρ_e) of the sample was determined using the principle of Archimedes. The Dulong-Petit model was employed to estimate the heat capacity (C_p). The κ_{tot} was calculated by $\kappa_{\text{tot}} = DC_p\rho_e$. The Hall coefficient of the sample was measured at room temperature by a homemade test apparatus (magnetic field range of ± 1 T). The Hall n_H and carrier mobility (μ_H) at room temperature were calculated using $n_H = 1/eR_H$ and $\mu_H = \sigma R_H$, respectively, where e stands for the number of electron charges and σ represents conductivity. The transverse sound velocity (v_t) and longitudinal sound velocity (v_l) of the sample were measured by an ultrasonic pulse receiver (5073PR, OLYMPUS).

RESULTS AND DISCUSSION

To confirm the phase purity of the samples after ball-milling and hot-pressing, X-ray diffraction (XRD) measurements were conducted for all samples. The XRD patterns of each sample are shown in [Figure 1A](#). The sample's primary peaks correspond well to the tetragonal stannite structure (ICSD#155904) and then conducted local amplifications of the XRD patterns for all samples [[Supplementary Figure 1](#)]. The XRD peaks did indeed shift by a certain angle, as expected. To further ascertain the crystalline structure of the sample, taking S-5 as an example, using Fullprof software for Rietveld refinements [[Figure 1B](#)]. The Rietveld refinements calculation details for the remaining samples are presented in [Supplementary Figure 2](#). The lattice parameters of all samples along the z and x axes (c and a) showed a slight change [[Figure 1C](#)], which is caused by the locality of point defects resulting from Te replacing Se and the low Te doping content. This phenomenon has also been observed in other quaternary chalcogenides^[21,30,31]. The structure distortion parameters of all samples were calculated based on the lattice parameters calculated by Rietveld refinements, as shown in [Figure 1D](#). Under the influence of the crystal field effect in quaternary chalcogenides, the triply degenerate valence band Γ_{15V} of the cubic zinc blende structure splits into a non-degenerate band Γ_{4V} and a doubly degenerate band Γ_{5V} , resulting in a splitting energy Δ_{CF} defined as $\Delta_{CF} = E(\Gamma_{5V}) - E(\Gamma_{4V})$. When η approaches 1, the sample displays high symmetry, and the Δ_{CF} will be closer to 0, which is more favorable for maintaining better electrical properties^[26]. All samples show η values above 0.98, indicating their high symmetry.

The microstructure of the fracture surface of the sample was studied using SEM, and the results are depicted in [Figure 2A-E](#). It was found that there are no obvious holes or cracks in all the samples within the entire

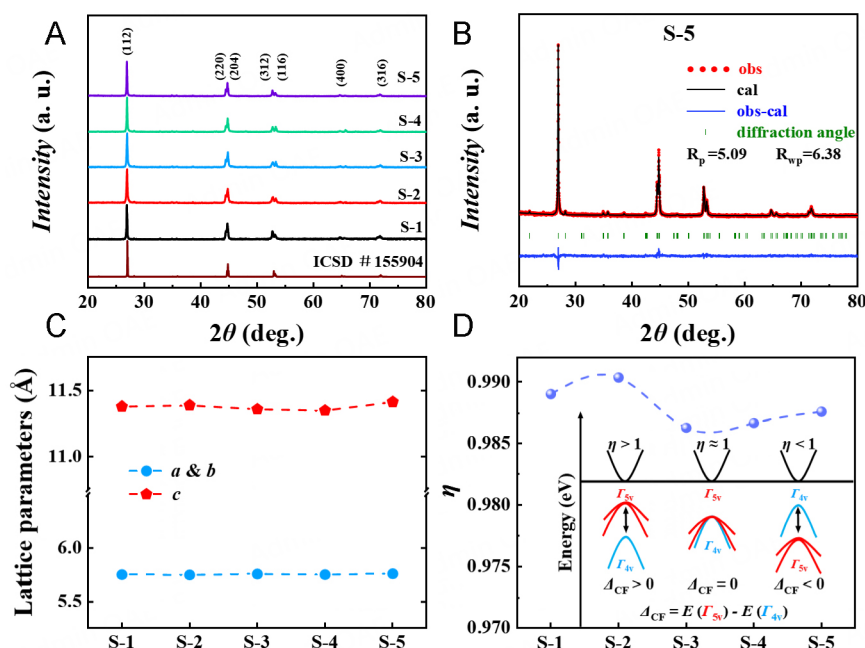


Figure 1. (A) Samples powder XRD pattern at room temperature (B) Rietveld refinement of S-5 with Fullprof software (C) The lattice parameters (a & b , c) of samples, (D) The relationship between structure distortion parameters η and band structure of samples^[19].

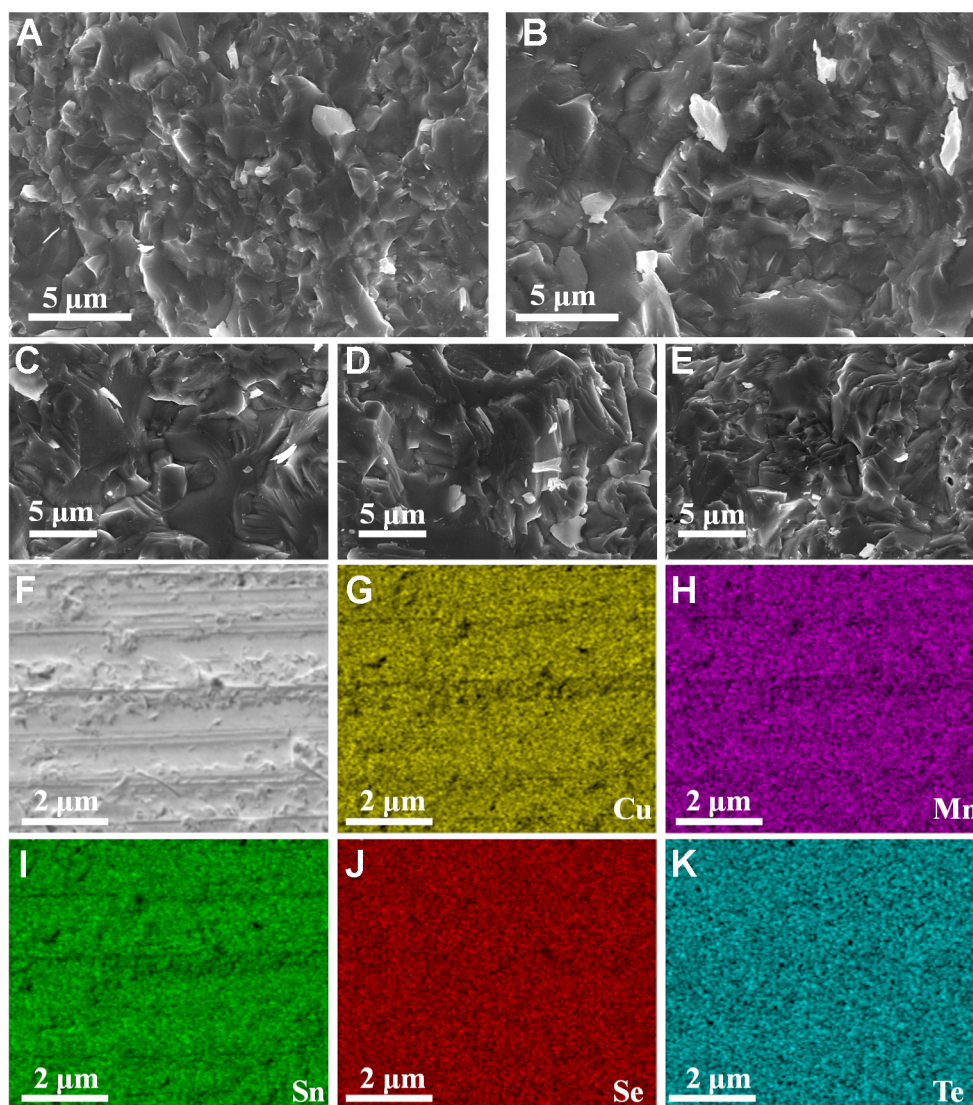
scanning range and the grain size of the samples is less than five micrometers. These results show that the synthesized sample has a high density ($\geq 96\%$), which corresponds to the high density measured in the experiment [Table 1]. To investigate the uniformity of element distribution in the sample, energy dispersive spectroscopy (EDS) analysis was conducted with S-5 as an example. As shown in Figure 2F–K, all elements Cu, Mn, Sn, Se and Te were uniformly distributed with no significant aggregation or dispersion observed. Additionally, the mass fraction of each element was provided in the Supplementary Figure 3.

XPS was used to analyze the valence states of elements in S-5. As shown in Figure 3, Cu 2p showed two peaks at 931.4 and 951.3 eV [Figure 3A], corresponding to the valence state of Cu^{+} ^[19]. The Mn 2p_{3/2} binding energy peak was observed at 640.8 eV, while the Mn 2p_{1/2} peak was observed at 653.3 eV [Figure 3B], which is also the case in $\text{Cu}_2\text{MnSnSe}_4$ ^[19] and XPS study of Mn^{2+} ^[32]. It can be concluded that the valence state of Mn in the sample is +2. Sn 3d_{5/2} and Sn 3d_{3/2} binding energy peaks were observed at 485.8 and 494.5 eV, respectively [Figure 3C], with no other significant peaks. In $\text{Cu}_2\text{ZnSnSe}_4$ ^[33], the binding energy peak of Sn 3d_{5/2} is about 486 eV, indicating that Sn shows +4 valence. The Se 3d showed two peaks at 54 and 59.2 eV [Figure 3D], corresponding to the valence state of Se^{2-} ^[16,30]. Comparison of the Se XPS peaks for the S-2 and S-5 samples and find that the peak shift observed in the S-5 sample [Supplementary Figure 4] proves the successful doping of Te. Supplementary Figure 1 further supports this conclusion. As for the measurement of the valence state of Te, due to the low content of Te in the sample, the Te signal is easily obscured by background noise during the XPS measurement, resulting in an indistinct peak shape. However, the above results from local amplifications of the XRD patterns [Supplementary Figure 1] and XPS have indicated the presence of Te^{2-} .

Figure 4 shows the electrical performance measurement results of all samples. At 473 K, the σ of all samples reached its maximum value. Specifically, the σ for S-2 is $4.27 \times 10^4 \text{ S m}^{-1}$, and for S-5, it is $1.56 \times 10^4 \text{ S m}^{-1}$ at 473 K [Figure 4A]. At around 470 K, the σ shows a non-monotonic change; unlike the decrease in σ at high temperatures caused by thermally activated charge carriers in some functional materials^[34], this change in

Table 1. The lattice parameters (a & b , c), cell volume (V), structure distortion parameter (η), experimental density (ρ_e), theoretical density (ρ_t), relative density (ρ_r), carrier concentration (n_H) and carrier mobility (μ_H) of all samples at room temperature

	S-1	S-2	S-3	S-4	S-5
a & b (Å)	5.752(6)	5.749(6)	5.758(7)	5.751(9)	5.759(8)
c (Å)	11.378(6)	11.388(1)	11.359(3)	11.350(5)	11.376(6)
V (Å ³)	376.55	376.48	376.71	375.53	377.43
η	0.9890	0.9903	0.9863	0.9867	0.9876
ρ_e (g cm ⁻³)	5.3974	5.4309	5.4383	5.4397	5.1705
ρ_t (g cm ⁻³)	5.45195	5.4857	5.4932	5.4946	5.3859
ρ_r (%)	99	99	99	99	96

**Figure 2.** SEM results of (A) S-1, (B) S-2, (C) S-3, (D) S-4, (E) S-5 and (F-K) EDS results for S-5.

conductivity behavior may be due to the transition from Cu ordered state to Cu disordered state^[16]. With the doping of Te, the sample conductivity decreases continuously. Hall effect test at room temperature

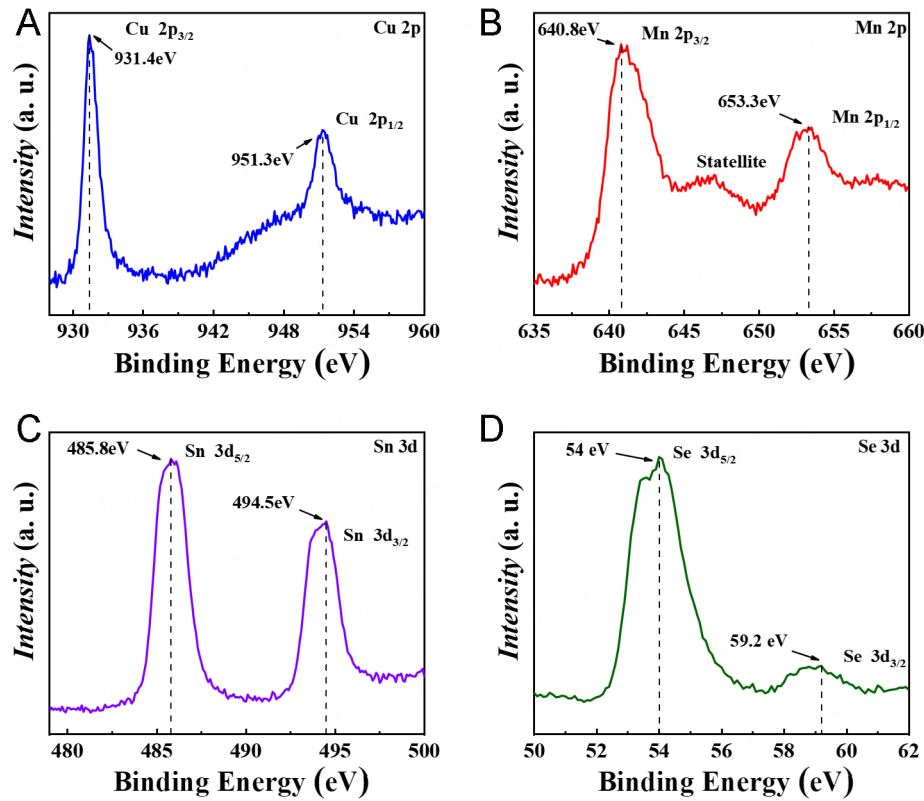


Figure 3. X-ray photoelectron spectroscopy of S-5: (A) Cu 2p (B) Mn 2p (C) Sn 3d (D) Se 3d.

[Figure 4B] was conducted to determine the reason for the change in conductivity. The heterovalent substitution of Mn by Cu in S-2 led to an increase in both n_H and μ_H ; the n_H of S-2 is significantly increased compared to that of the S-1 sample (from 1.66 to 3.38 cm^{-3}), resulting in an enhancement in conductivity. With the doping of Te, the n_H of the samples (S-3 to S-5) fluctuates in the range of 4.1×10^{19} and $3.9 \times 10^{19} \text{ cm}^{-3}$, according to the findings of Zhang *et al.*, in $\text{Cu}_{2.1}\text{Mn}_{0.9}\text{SnSe}_4$, the Cu vacancy defect is the main defect, so it is speculated that the fluctuation of n_H is due to the change of Cu vacancy concentration caused by Te doping^[26]. Following Te doping, the μ_H of the sample decreases, primarily due to an increase in point defects; the scattering centers are formed within the material, which scatters the movement of the carrier, thus reducing the μ_H .

Figure 4C illustrates the relationship between the Seebeck coefficients (S) and temperature. All S exhibit positive values, suggesting that holes serve as the primary charge carriers. The S values of S-2 to S-5 are lower than those of S-1, due to the increase of n_H . At 673 K, S-5 obtains a maximum S of $219 \mu\text{V K}^{-1}$ in the doped sample. The PF of each sample was calculated using $PF = S^2\sigma$, and the temperature dependence of each sample's PF was shown in Figure 4D. The PF of all the samples showed a monotonic temperature dependence, with the PF increasing with the temperature. At 673 K, the doped samples exhibit a higher PF compared to the undoped samples. In the low-temperature region (less than 450 K), the PF of S-2 to S-4 was almost the same, while the PF of S-5 remained high. With the temperature increase, the PF of S-2 further rises, reaching a maximum of $663 \mu\text{W m}^{-1} \text{ K}^{-2}$ at 673 K. The temperature dependence of the PF of S-2 and S-3 is nearly identical, except at 623 K.

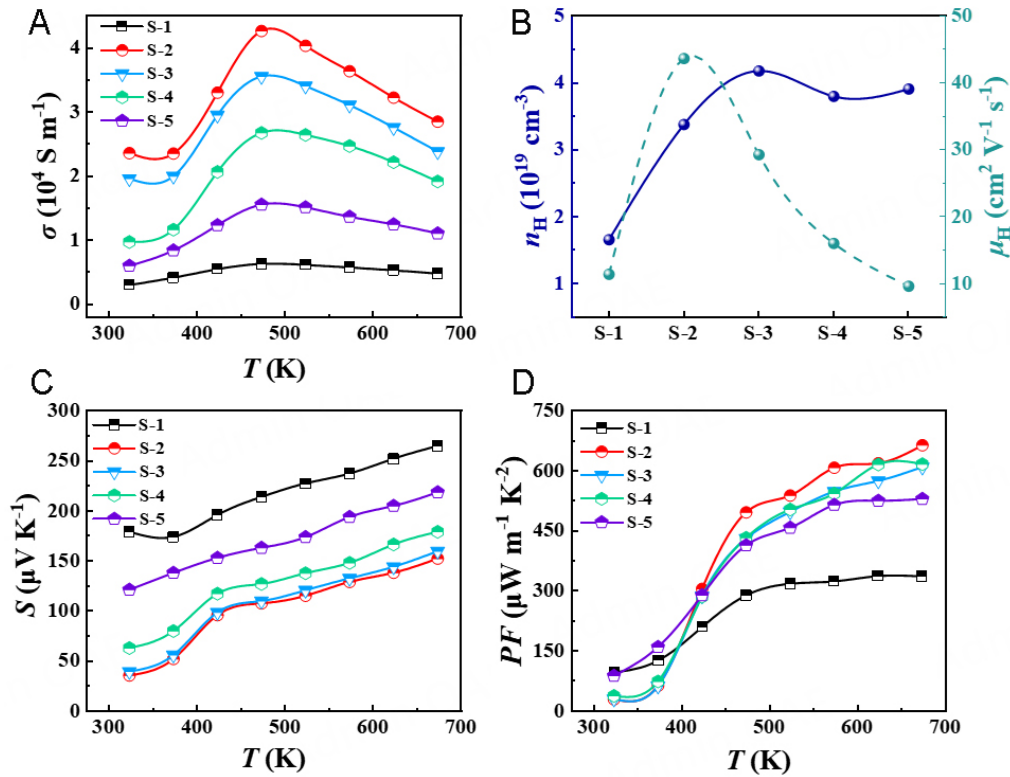


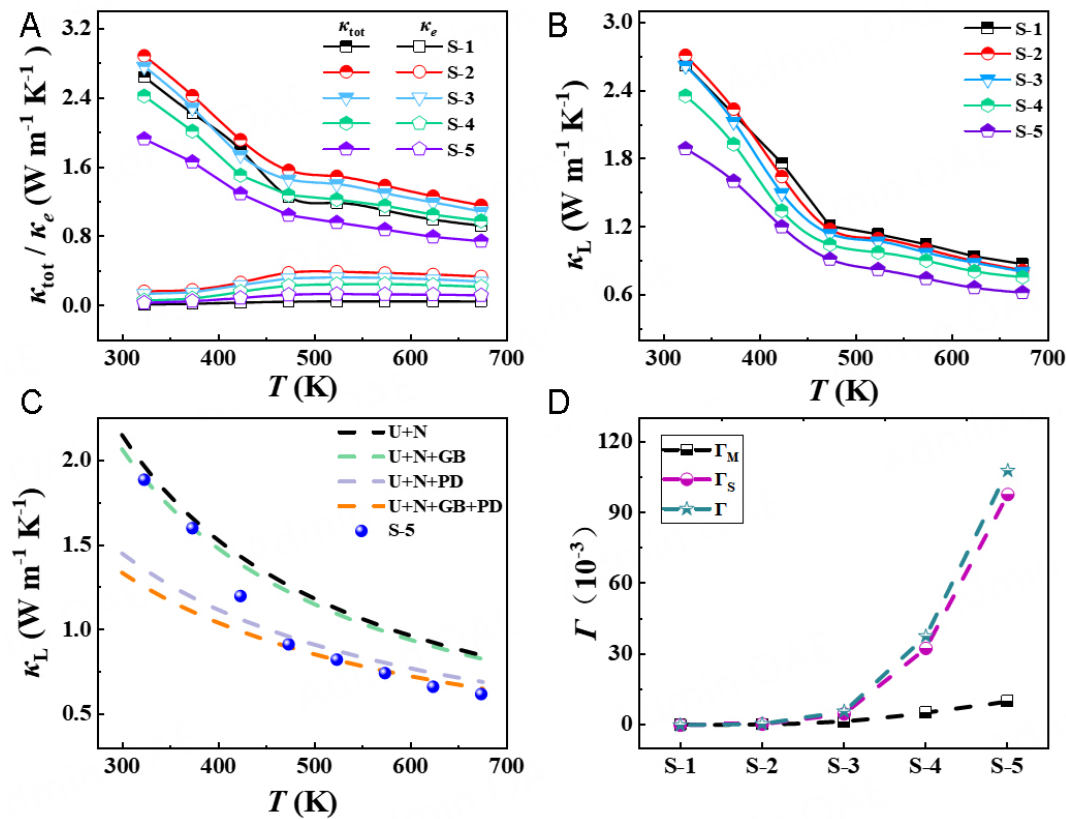
Figure 4. Temperature dependences of (A) the electrical conductivity (σ), (C) the Seebeck coefficient (S) and (D) the power factor (PF) for all samples. (B) the room temperature Hall carrier concentration (n_H) and mobility (μ_H) for all samples.

Figure 5A shows that the κ_{tot} of the samples exhibits a decreasing trend throughout the measured temperature range (consistent with the trend of changes in the thermal diffusivity coefficient (D), Supplementary Figure 5). In non-stoichiometric sample (S-2), as the Te doping content increases (S-3 to S-5), the κ_{tot} is greatly reduced in the low-temperature region (below 450 K), and the decline slows down in the high-temperature region (above 450 K). For example, κ_{tot} decreases from $2.89 \text{ W m}^{-1} \text{ K}^{-1}$ of S-2 to $1.92 \text{ W m}^{-1} \text{ K}^{-1}$ of S-5 at 323 K, a reduction of $0.97 \text{ W m}^{-1} \text{ K}^{-1}$. Similarly, it decreases from $1.16 \text{ W m}^{-1} \text{ K}^{-1}$ of S-2 to $0.75 \text{ W m}^{-1} \text{ K}^{-1}$ of S-5 at 673 K, a reduction of $0.41 \text{ W m}^{-1} \text{ K}^{-1}$. At 323 K, S-5 achieved a minimum κ_{tot} of $1.92 \text{ W m}^{-1} \text{ K}^{-1}$, and at 673 K, it reached $0.75 \text{ W m}^{-1} \text{ K}^{-1}$. The Wiedemann-Franz formula can be utilized to compute the electron thermal conductivity ($\kappa_e = L\sigma T$, Supplementary Figure 6). As shown in Figure 5A, the κ_e increases first and then decreases within the measured temperature region. At 523 K, S-5 achieves a peak κ_e of $0.14 \text{ W m}^{-1} \text{ K}^{-1}$, which decreases to $0.12 \text{ W m}^{-1} \text{ K}^{-1}$ at 673 K. It is clear that the contribution of the κ_e to the κ_{tot} is very small. The κ_L of the samples can be obtained by $\kappa_L = \kappa_{\text{tot}} - \kappa_e$ [Figure 5B]. At 323 K, S-5 exhibits a κ_L of $1.9 \text{ W m}^{-1} \text{ K}^{-1}$, which is about 34% lower than that of S-2. Finally, S-5 exhibits the lowest κ_L of $0.6 \text{ W m}^{-1} \text{ K}^{-1}$ at 673 K across the entire measured temperature region, which is a low level among some quaternary chalcogenides^[16,21,35,36]. Within the entire measured temperature range, the κ_L decreases by 25% to 30%, suggesting that within a certain defect concentration range, the κ_L decreases as the defect concentration increases.

To further explore the reasons for the change of thermal conductivity, ultrasonic measurement was conducted on all samples, and the results are shown in Table 2. The average sound velocity (v_a), Grüneisen parameter (γ), mean free path of phonons (l_{ph}), the heat capacity (C_p) and Debye temperature (θ_D) were calculated for all samples (the relevant calculation details are shown in Supplementary Material). It is

Table 2. The transverse sound velocity (v_t), longitudinal sound velocity (v_l), average sound velocity (v_a), Debye temperatures (θ_D), Grüneisen parameter (γ), mean free path of phonons (l_{ph}) and specific heat capacity (C_p) for all samples at room temperature

	S-1	S-2	S-3	S-4	S-5
v_t (m s ⁻¹)	1,938	1,943	1,882	1,959	1,818
v_l (m s ⁻¹)	3,607	3,871	3,609	3,840	3,521
v_a (m s ⁻¹)	2,164	2,180	2,106	2,195	2,036
θ_D	225	227	219	229	211
γ	1.75	1.99	1.86	1.93	1.89
l_{ph} (nm)	2.07	2.12	2.12	1.83	1.68
C_p (J g ⁻¹ K ⁻¹)	0.32	0.32	0.32	0.32	0.32

**Figure 5.** The dependence of various thermal conductivity on temperature for all samples: (A) the total thermal conductivity (κ_{tot}) and electron thermal conductivity (κ_e), (B) the lattice thermal conductivity (κ_L) for all samples. (C) The theoretical κ_L of S-5 calculated based on Debye-Callaway model. (D) The total disorder parameter (Γ), the mass fluctuation parameter (Γ_M) and strain field fluctuation parameter (Γ_S) for all samples.

evident from Table 2 that the v_a of all samples remains nearly constant, and the heat capacity remains unchanged at $0.32 \text{ J g}^{-1} \text{ K}^{-1}$. According to $l_{ph} = 3\kappa_L / \rho C_p v_a$, the κ_L decreases mainly due to the reduction of l_{ph} . S-2 and S-3 have the same l_{ph} . Observing from Figure 5B, it is evident that the κ_L for S-2 and S-3 displays a similar trend of variation. As T continues to rise, the l_{ph} of S-4 and S-5 diminishes, resulting in a decrease in κ_L . This suggests that the scattering effect of defects on phonons becomes increasingly pronounced, thereby contributing to the reduction in κ_L . S-5 has the shortest l_{ph} (1.68 nm).

Theoretical simulations of the experimental κ_L were conducted using the Debye-Callaway model, with phonon-phonon Umklapp scattering (U), Normal scattering (N), grain boundary scattering (GB) and point defects scattering (PD) as the primary scattering mechanisms. In the Debye-Callaway model, the κ_L of a material can be expressed as:

$$\kappa_L = \frac{k_B}{2\pi^2 v_d} \left(\frac{k_B T}{\hbar} \right)^3 \int_0^{\theta_D/T} \frac{x^4 e^x}{\tau_c^{-1} (e^x - 1)^2} dx, x = \hbar\omega/k_B T$$

Phonon relaxation time is the result of multiple scattering mechanisms, which can be expressed as:

$$\tau_c^{-1} = \tau_U^{-1} + \tau_N^{-1} + \tau_{GB}^{-1} + \tau_{PD}^{-1}$$

where k_B is the Boltzmann constant; \hbar is Planck's constant; ω is the phonon frequency; τ_c is the relaxation time (the relevant calculation details are shown in [Supplementary Material](#)). The existence of phase transitions in the samples may affect the propagation speed and scattering probability of phonons, so the experimental data were fitted in segments. Taking S-5 as an example, a theoretical simulation of the experimental κ_L was conducted through the Debye model [Figure 5C]. In the low-temperature region (less than 450 K), the experimental results for S-5 align well with the green dashed line (U + N + GB), indicating that U, N, and GB are the primary scattering mechanisms in this temperature range. In the higher-temperature region (more than 450 K), the experimental results for S-5 align well with the orange dashed line (U + N + GB + PD), suggesting that point defect scattering gradually becomes one of the main scattering mechanisms. By directly comparing the four different dashed lines, it is noticeable that point defects significantly contribute to the decrease in κ_L .

With the increase of defect concentration, the mass and strain field fluctuations will be further induced, which will affect the total disorder of the crystal. $\Gamma = \Gamma_M + \Gamma_S$, where Γ is the total disorder parameter, Γ_M is the mass fluctuation parameter and Γ_S is the strain field fluctuation parameter (the relevant calculation details of Γ_M and Γ_S are shown in [Supplementary Material](#)). Figure 5D illustrates the variation of the mass fluctuation parameter and the strain field fluctuation parameter. It is evident that both Γ_M and Γ_S increase with the Te, and for each set of samples, the value of Γ_S exceeds Γ_M , suggesting that the strain field fluctuation scattering make the primary contribution to reducing κ_L . Since the atomic radius of Te is larger than that of Se, the substitution of Se by Te leads to deviations in atomic positions and thus increasing local lattice distortions. This is the main reason for why Γ_S is greater than Γ_M . In conclusion, these factors can well explain the contribution of point defects to the decrease of κ_L .

The relationship between the zT and temperature is shown in Figure 6A. After Te doping, zT is significantly enhanced throughout the measured temperature range due to the optimized PF and low κ_L . Finally, S-5 achieves the maximum $zT \sim 0.5$ at 673 K, roughly twice that of the S-1. [Supplementary Figure 7](#) compares the thermoelectric properties between $\text{Cu}_{2.1}\text{Mn}_{0.9}\text{SnSe}_{3.9}\text{Te}_{0.2}$ and $\text{Cu}_{2.1}\text{Mn}_{0.9}\text{SnSe}_{3.9}\text{Te}_{0.1}$ [Supplementary Figure 7]. The results indicate that, within the $\text{Cu}_{2.1}\text{Mn}_{0.9}\text{SnSe}_{4-x}\text{Te}_x$ samples, the compound with $x = 0.1$ exhibits the optimal thermoelectric performance. Figure 6B presents the maximum zT achieved by some other $\text{Cu}_2\text{MnSnSe}_4$ systems at 673 K. This work attained a relatively high zT among $\text{Cu}_2\text{MnSnSe}_4$ systems, as can be easily observed.

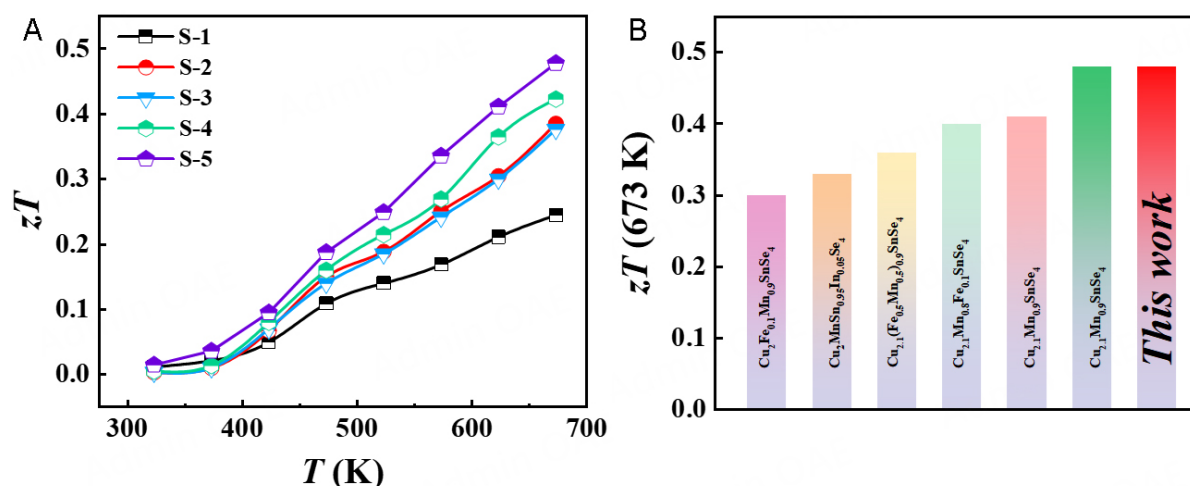


Figure 6. (A) Temperature dependence of the dimensionless figure of merit (zT) for all the samples. (B) Comparison of zT for S-5 and other $\text{Cu}_2\text{MnSnSe}_4$ systems^[21,27-29,37,38] at 673 K.

CONCLUSIONS

In this work, a series of samples, including $\text{Cu}_2\text{MnSnSe}_4$ (S-1) and $\text{Cu}_{2.1}\text{Mn}_{0.9}\text{SnSe}_{4-x}\text{Te}_x$ ($x = 0, 0.01, 0.05, 0.10$; S-2 to S-5), were successfully synthesized by ball-milling and hot-pressing methods, and their structural components and electrothermal transport properties were studied. Rietveld refinement and SEM showed that all samples are tetragonal stannite structures with high density. XPS showed that Te doping does not change the valence states of the sample elements. The increase of n_{H} leads to elevation of the σ in S-5, and the PF of S-5 reaches $530 \mu\text{W m}^{-1} \text{K}^{-2}$ at 673 K. As the doping content of Te increases, the defect concentration in the samples also rises, resulting in enhanced scattering effects on phonons, thus reducing the l_{ph} and hindering phonon transport, which significantly reduces the κ_{L} . At 673 K, S-5 reaches a minimum κ_{L} of $0.62 \text{ W m}^{-1} \text{K}^{-1}$. Due to the improvement of PF and the decrease of κ_{L} , S-5 reaches $zT \sim 0.5$, which is about twice that of the S-1 at 673 K. Therefore, it can be shown that the introduction of Te can further improve the thermoelectric performance of $\text{Cu}_2\text{MnSnSe}_4$ -based compounds.

DECLARATIONS

Authors' contributions

Writing original draft and Data curation: Liu, F.

Manuscript revision: Sun, Y.; Li, Z.; Peng, P.

Supervision and Resources: Wang, C.; Wang, H.

Availability of data and materials

The data supporting the findings of this study are available within this Article and its [Supplementary Material](#). Further data are available from the corresponding authors upon request.

Financial support and sponsorship

The work is financially supported by the Natural Science Fund of China under Grant Nos. 52171216 and 52472221, Qilu Young Scholar Program of Shandong University and Core Facility Sharing Platform of Shandong University.

Conflicts of interest

All authors declared that there are no conflicts of interest.

Ethical approval and consent to participate

Not applicable.

Consent for publication

Not applicable.

Copyright

© The Author(s) 2025.

REFERENCES

1. Wang, X.; Wang, Y.; Wu, M.; Fang, R.; Yang, X.; Wang, D. Ultrasonication-assisted fabrication of porous ZnO@C nanoplates for lithium-ion batteries. *Microstructures* **2022**, *2*, 2022016. [DOI](#)
2. Zhang, S. High entropy design: a new pathway to promote the piezoelectricity and dielectric energy storage in perovskite oxides. *Microstructures* **2023**, *3*, 2023003. [DOI](#)
3. Liu, X.; Webb, T.; Dai, L.; et al. Influence of halide choice on formation of low-dimensional perovskite interlayer in efficient perovskite solar cells. *Energy. Environ. Mater.* **2022**, *5*, 670-82. [DOI](#)
4. Bell, L. E. Cooling, heating, generating power, and recovering waste heat with thermoelectric systems. *Science* **2008**, *321*, 1457-61. [DOI](#) [PubMed](#)
5. Xiao, Y.; Zhao, L. D. Seeking new, highly effective thermoelectrics. *Science* **2020**, *367*, 1196-7. [DOI](#)
6. Cao, T.; Shi, X. L.; Zou, J.; Chen, Z. G. Advances in conducting polymer-based thermoelectric materials and devices. *Microstructures* **2021**, *1*, 2021007. [DOI](#)
7. Mao, J.; Zhu, H.; Ding, Z.; et al. High thermoelectric cooling performance of n-type Mg_3Bi_2 -based materials. *Science* **2019**, *365*, 495-8. [DOI](#)
8. Snyder, G. J.; Toberer, E. S. Complex thermoelectric materials. *Nat. Mater.* **2008**, *7*, 105-14. [DOI](#) [PubMed](#)
9. Vijay, V.; Harish, S.; Archana, J.; Navaneethan, M. Synergistic effect of grain boundaries and phonon engineering in Sb substituted Bi_2Se_3 nanostructures for thermoelectric applications. *J. Colloid. Interface. Sci.* **2022**, *612*, 97-110. [DOI](#) [PubMed](#)
10. Wu, Y.; Nan, P.; Chen, Z.; et al. Manipulation of band degeneracy and lattice strain for extraordinary PbTe thermoelectrics. *Research* **2020**, *2020*, 8151059. [DOI](#) [PubMed](#) [PMC](#)
11. Kim, S. I.; Lee, K. H.; Mun, H. A.; et al. Dense dislocation arrays embedded in grain boundaries for high-performance bulk thermoelectrics. *Science* **2015**, *348*, 109-14. [DOI](#)
12. Liu, W. D.; Wang, D. Z.; Liu, Q.; Zhou, W.; Shao, Z.; Chen, Z. G. High-performance GeTe-based thermoelectrics: from materials to devices. *Adv. Energy. Mater.* **2020**, *10*, 2000367. [DOI](#)
13. Han, M. K.; Yu, B. G.; Jin, Y.; Kim, S. J. A synergistic effect of metal iodide doping on the thermoelectric properties of Bi_2Te_3 . *Inorg. Chem. Front.* **2017**, *4*, 881-8. [DOI](#)
14. Feng, L.; Guo, A.; Liu, K.; et al. Highly deformable $\text{Ag}_2\text{Te}_{1-x}\text{Se}_x$ -based thermoelectric compounds. *Mater. Today. Phys.* **2023**, *33*, 101051. [DOI](#)
15. Heremans, J. P.; Jovovic, V.; Toberer, E. S.; et al. Enhancement of thermoelectric efficiency in PbTe by distortion of the electronic density of states. *Science* **2008**, *321*, 554-7. [DOI](#)
16. Zheng, J.; Hong, T.; Wang, D.; Qin, B.; Gao, X.; Zhao, L. Synergistically enhanced thermoelectric properties in n-type $\text{Bi}_6\text{Cu}_2\text{Se}_4\text{O}_6$ through inducing resonant levels. *Acta. Mater.* **2022**, *232*, 117930. [DOI](#)
17. Zhang, Z.; Zhao, K.; Chen, H.; et al. Entropy engineering induced exceptional thermoelectric and mechanical performances in $\text{Cu}_{2-y}\text{Ag}_y\text{Te}_{1-2x}\text{S}_x\text{Se}_x$. *Acta. Mater.* **2022**, *224*, 117512. [DOI](#)
18. Hu, L.; Zhang, Y.; Wu, H.; et al. Entropy engineering of SnTe: multi-principal-element alloying leading to ultralow lattice thermal conductivity and state-of-the-art thermoelectric performance. *Adv. Energy. Mater.* **2018**, *8*, 1802116. [DOI](#)
19. Sun, Y.; Wang, H.; Yao, J.; et al. High symmetry structure and large strain field fluctuation lead enhancement of thermoelectric performance of quaternary alloys by tuning configurational entropy. *Chem. Eng. J.* **2023**, *462*, 142185. [DOI](#)
20. Liu, M.; Sun, Y.; Zhu, J.; et al. High performance GeTe thermoelectrics enabled by lattice strain construction. *Acta. Mater.* **2023**, *244*, 118565. [DOI](#)
21. Song, Q.; Qiu, P.; Chen, H.; et al. Enhanced carrier mobility and thermoelectric performance in $\text{Cu}_2\text{FeSnSe}_4$ diamond-like compound via manipulating the intrinsic lattice defects. *Mater. Today. Phys.* **2018**, *7*, 45-53. [DOI](#)
22. Zhang, Y. X.; Lou, Q.; Ge, Z. H.; et al. Excellent thermoelectric properties and stability realized in copper sulfides based composites via complex nanostructuring. *Acta. Mater.* **2022**, *233*, 117972. [DOI](#)
23. Zhuang, H. L.; Hu, H.; Pei, J.; et al. High ZT in p-type thermoelectric $(\text{Bi,Sb})_2\text{Te}_3$ with built-in nanopores. *Energy. Environ. Sci.* **2022**,

- 15, 2039-48. DOI
24. Wang, T.; Huo, T.; Wang, H.; Wang, C. Quaternary chalcogenides: promising thermoelectric material and recent progress. *Sci. China. Mater.* **2020**, *63*, 8-15. DOI
25. Song, Q.; Qiu, P.; Hao, F.; et al. Quaternary Pseudocubic $\text{Cu}_2\text{TMSnSe}_4$ (TM = Mn, Fe, Co) chalcopyrite thermoelectric materials. *Adv. Elect. Mater.* **2016**, *2*, 1600312. DOI
26. Zhang, J.; Liu, R.; Cheng, N.; et al. High-performance pseudocubic thermoelectric materials from non-cubic chalcopyrite compounds. *Adv. Mater.* **2014**, *26*, 3848-53. DOI
27. Song, Q.; Qiu, P.; Chen, H.; et al. Improved thermoelectric performance in nonstoichiometric $\text{Cu}_{2+\delta}\text{Mn}_{1-\delta}\text{SnSe}_4$ quaternary diamondlike compounds. *ACS. Appl. Mater. Interfaces.* **2018**, *10*, 10123-31. DOI
28. Mehmood, F.; Sun, Y.; Su, W.; et al. Improved thermoelectric performance of in-doped quaternary $\text{Cu}_2\text{MnSnSe}_4$ alloys. *Phys. Status. Solidi.* **2022**, *16*, 2200049. DOI
29. Sun, Y.; Abbas, A.; Wang, H.; et al. Enhancement of thermoelectric performance of $\text{Cu}_2\text{MnSnSe}_4$ alloys by regulation of lattice strain. *Chem. Eng. J.* **2024**, *486*, 150158. DOI
30. Mukherjee, B.; Isotta, E.; Malagutti, M. A.; et al. Thermoelectric performance in disordered $\text{Cu}_2\text{ZnSnSe}_4$ nanostructures driven by ultra-low thermal conductivity. *J. Alloys. Compd.* **2023**, *933*, 167756. DOI
31. Chen, Q.; Yan, Y.; Zhan, H.; et al. Enhanced thermoelectric performance of chalcogenide $\text{Cu}_2\text{CdSnSe}_4$ by ex-situ homogeneous nanoinclusions. *J. Materiomics.* **2016**, *2*, 179-86. DOI
32. Cheng, Y.; Qumu, G.; Huang, T.; Miao, A.; Wen, G. Potassium ferrate enhanced active manganese oxide filter material to remove BPA: influence of NH_4^+ , Mn^{2+} . *Sep. Purif. Technol.* **2024**, *341*, 126903. DOI
33. Henríquez, R.; Salazar Nogales, P.; Grez Moreno, P.; et al. Solvothermal synthesis of $\text{Cu}_2\text{ZnSnSe}_4$ nanoparticles and their visible-light-driven photocatalytic activity. *Nanomaterials* **2024**, *14*, 1079. DOI PubMed PMC
34. Xie, S.; Xu, Q.; Chen, Q.; Zhu, J.; Wang, Q. Realizing super-high piezoelectricity and excellent fatigue resistance in domain-engineered bismuth titanate ferroelectrics. *Adv. Funct. Mater.* **2024**, *34*, 2312645. DOI
35. Chetty, R.; Bali, A.; Mallik, R. C. Thermoelectric properties of indium doped $\text{Cu}_2\text{CdSnSe}_4$. *Intermetallics* **2016**, *72*, 17-24. DOI
36. Wei, K.; Nolas, G. S. Synthesis and characterization of nanostructured stannite $\text{Cu}_2\text{ZnSnSe}_4$ and $\text{Ag}_2\text{ZnSnSe}_4$ for thermoelectric applications. *ACS. Appl. Mater. Interfaces.* **2015**, *7*, 9752-7. DOI PubMed
37. Song, Q.; Qiu, P.; Zhao, K.; Deng, T.; Shi, X.; Chen, L. Crystal structure and thermoelectric properties of $\text{Cu}_2\text{Fe}_{1-x}\text{Mn}_x\text{SnSe}_4$ diamond-like chalcogenides. *ACS. Appl. Energy. Mater.* **2020**, *3*, 2137-46. DOI
38. Dong, Y.; Wojtas, L.; Martin, J.; Nolas, G. S. Synthesis, crystal structure, and transport properties of quaternary tetrahedral chalcogenides. *J. Mater. Chem. C.* **2015**, *3*, 10436-41. DOI